PHYSICS

Small-scale roughness entraps water and controls underwater adhesion

Nityanshu Kumar[1], Siddhesh Dalvi[1], Anirudha V. Sumant[2], Lars Pastewka[3,4], Tevis D. B. Jacobs[5], Ali Dhinojwala[1]*

While controlling underwater adhesion is critical for designing biological adhesives and in improving the traction of tires, haptics, or adhesives for health monitoring devices, it is hindered by a lack of fundamental understanding of how the presence of trapped water impedes interfacial bonding. Here, by using well-characterized polycrystal diamond surfaces and soft, nonhysteretic, low–surface energy elastomers, we show a reduction in adhesion during approach and four times higher adhesion during retraction as compared to the thermodynamic work of adhesion. Our findings reveal how the loading phase of contact is governed by the entrapment of water by ultrasmall (10-nanometer-scale) surface features. In contrast, the same nanofeatures that reduce adhesion during approach serve to increase adhesion during separation. The explanation for this counterintuitive result lies in the incompressibility-inextensibility of trapped water and the work needed to deform the polymer around water pockets. Unlike the well-known viscoelastic contribution to adhesion, this science unlocks strategies for tailoring surface topography to enhance underwater adhesion.

INTRODUCTION

Geckos running up wet inclined surfaces or mussels sticking to rocks in turbulent ocean waters demonstrate how natural systems overcome the presence of water, which destroys the function of most commercial adhesives (*1*–*4*). Underwater adhesion is important for the design of vehicle tires with improved traction on wet roads, effective biological adhesives to replace surgical sutures, or health-monitoring sensors that can function in the presence of water and humidity.

For smooth ideal surfaces, the underwater contact is influenced by surface chemistry and the water drainage rate (*5*). For example, underwater work of adhesion increases with hydrophobicity and can be determined by using the Young-Dupré equation, which is a function of the interfacial energies (*5*, *6*). The interfacial energy of hydrophobic surfaces in water is higher than when in contact with air, thus increasing their underwater work of adhesion. However, the drainage of water is almost a thousandfold slower for hydrophobic surfaces compared to hydrophilic surfaces in conditions where water is trapped during fast approach (*5*, *6*).

In real-world scenarios, most surfaces are rough at many length scales, and the contact interface may not be conformal but may contain regions of trapped air or water. For rough surfaces in dry conditions, the work of adhesion during the approach may be determined using the Persson-Tosatti model (*7*). This model assumes that the final state is conformal, and the apparent work of adhesion is lower than the ideal thermodynamic work of adhesion by the amount of elastic energy required to conform to the roughness of the solid surface. This model has been successful in predicting the work of adhesion during the approach for smooth elastic rubber in contact with rough diamond surfaces (*6*, *7*). However, the model has not been successful in predicting the work of adhesion in separating two surfaces. For heterogeneous contact (roughness or chemical), the contact line is pinned during retraction, and detachment occurs in the form of localized instantaneous jumps (*8*, *9*). This detachment follows Griffith's criterion, which states that these jumps occur only when the elastic energy released per unit area is equal to the interfacial energy or the energy required for the creation of new surfaces (*10*).

In underwater adhesion, the presence of roughness can lead to stable nonconformal contact with trapped water, and how adhesion relates to roughness in such complex systems has remained unresolved. These systems are much more common than ideal smooth surfaces, where adhesion can be explained by the classical Johnson-Kendall-Roberts (JKR) model. Biological systems control roughness using micro- and nanofeatures that are known to help in draining water and creating conformal contacts (*11*–*15*). However, nonconformal contacts are common under water, and we lack a theoretical framework to predict the actual contact area and the energy required for elastic deformation to create nonconformal contacts. In addition, the retraction may also be influenced by capillary forces, which are known to affect the adhesion of biological systems with controlled roughness (*16*–*20*). Therefore, it is critical to develop a fundamental understanding of how roughness affects underwater adhesion.

Here, we address the unresolved question of how underwater adhesion is affected by roughness and determine whether the contact interface is conformal and dry. Our experimental design is based on hydrophobic chemistry to create two surfaces, hydrogen-terminated (H-terminated) rough polycrystalline diamond and soft polydimethylsiloxane (PDMS) elastomer, to isolate the effect of roughness on underwater adhesion. This design reduces the influence of hydrogen or chemical bonds on the adhesion hysteresis (*6*, *21*). In addition, the PDMS chemistry with nearly complete cross-linking minimizes the influence of viscoelasticity (*7*). For rough surfaces, we use four topographically different diamond surfaces: microcrystalline diamond (MCD), nanocrystalline diamond (NCD), ultrananocrystalline diamond (UNCD), and a polished form of UNCD (PUNCD).

[1]School of Polymer Science and Polymer Engineering, The University of Akron, Akron, OH 44325, USA. [2]Center for Nanoscale Materials, Argonne National Laboratory, Lemont, IL 60439, USA. [3]Department of Microsystems Engineering, University of Freiburg, Freiburg 79110, Germany. [4]Cluster of Excellence livMatS, Freiburg Center for Interactive Materials and Bioinspired Technologies, University of Freiburg, Freiburg 79110, Germany. [5]Department of Mechanical Engineering and Materials Science, University of Pittsburgh, Pittsburgh, PA 15261, USA.
*Corresponding author. Email: ali4@uakron.edu

The roughness of these diamond substrates is well-characterized across eight orders of magnitude ranging from the size of the substrates (centimeters) to the angstrom scale (*22*). The height power spectral density (PSD) of a diamond substrate and the elastic modulus of PDMS are used to calculate the elastic energy required to conform to the rough surface and to calculate the true contact area, which can be used to test the theoretical predictions (*7*, *23*). We varied the elastic modulus of the smooth nonhysteretic PDMS elastomers from 0.7 to 9.2 MPa to test the influence of the modulus. The 16 different contact conditions (four substrates in contact with elastomers of four different moduli) and measurements of adhesion in both directions during approach and retraction and in the presence and absence of water allowed us to test the current theoretical model and propose a new nonconformal model to explain underwater adhesion.

RESULTS

The adhesion measurements were conducted by bringing a soft PDMS elastomer into contact with rough diamond surfaces in the presence of water using the geometry shown in Fig. 1A. The procedure for preparing the PDMS lenses is described in section S1. The characterization of diamond surface chemistry is described in section S2, and the calculation of the roughness parameters is presented in section S3. The hydrogen termination of diamond surfaces ensures the hydrophobic nature of the substrates and reduces adhesion hysteresis for smooth surfaces (*24*). For adhesion measurements, the radius of the contact spot was measured using an optical microscope. The loading measurements were performed quasi-statically, i.e., in a stepwise manner with a velocity of 60 nm/s between steps. For adhesive contact, the radius of the contact spot is higher than that predicted by Hertzian contact mechanics and described using the JKR model (dotted lines in Fig. 1B) (*25*). The adhesion data (W_{app}) obtained using JKR fits are summarized in tables S4 and S5 for the 16 contacts measured in both air and water. It is important to note that the JKR model with W_{app} which is independent of normal load was able to model the data in Fig. 1C. Because these measurements were conducted at low normal loads, we anticipate that the state of the contact region (amount of trapped water) does not

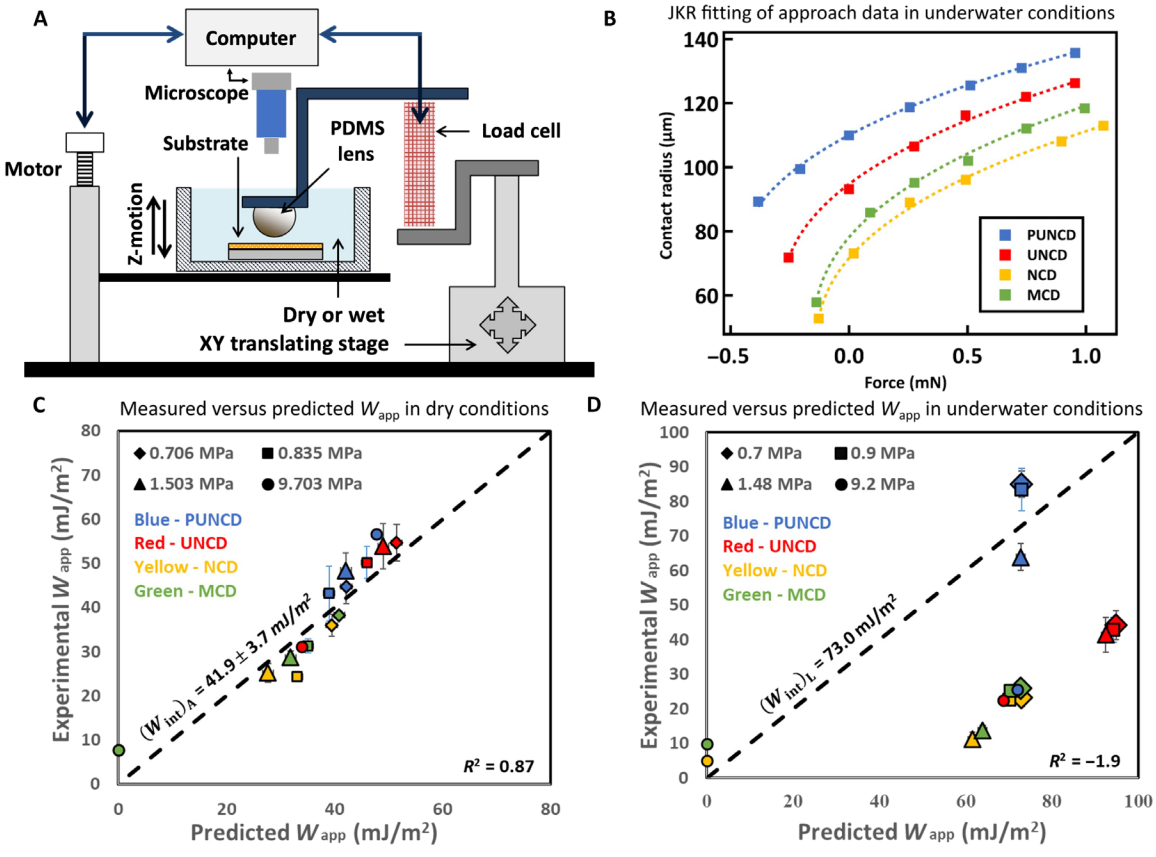

Fig. 1. Schematic of adhesion experiments and adhesion values in dry and wet conditions during approach. (**A**) Experimental geometry for measuring adhesion using the JKR model (*50*). (**B**) The contact radius of 0.9 MPa PDMS lens in contact with rough surfaces is plotted as a function of applied load (during approach) for underwater condition. To limit the amount of time the diamond surfaces are exposed to water, we measured contact radius during approach only, and not during retraction; during retraction, we only measured force. The dashed lines are fits using the JKR model in eq. S10. The Maugis parameter is much greater than 1, and JKR analysis is appropriate for modeling the adhesion data (section S4). The results from such fits are provided in table S4 (for dry case) and table S5 (for underwater case). Comparison of experimental work of adhesion between smooth elastic PDMS and rough rigid diamond contacts with those predicted using conformal model (Eq. 1). In dry conditions (**C**), the predictions show an excellent correlation ($R^2 = 0.87$) with experimental values for a $(W_{int})_A$ of ~42 mJ/m^2 (same as the thermodynamic expectations). In underwater conditions (**D**), the predictions are far from the $y = x$ line, suggesting that these contacts do not follow the conformal model. The $(W_{int})_L$ value of 73 mJ/m^2 was determined using Eq. 3.

change during the loading cycle. The actual radius of contact changes with load, and this is captured using the JKR model.

We compared the measured adhesion values during approach to those expected from the thermodynamic work of adhesion using the Persson-Tosatti contact mechanics model (*23*), which predicts that the apparent work of adhesion (W_{app}) for rough surfaces is affected by two factors. One factor increases W_{app} due to an increase in the real contact area as compared to the projected contact area, $r_{true} = A_{true}/A_{app}$. The second factor reduces W_{app} due to the elastic energy required to deform the soft elastomer. For a conformal contact, the roughness of a deformed elastomer is the same as that of the rough solid surface. W_{app} is expressed as

$$W_{app} = (W_{int})_{\alpha} r_{true} - \gamma_{PDMS-\alpha}(r_{true} - 1) - \frac{U_{elastic}}{A_{app}} \quad (1)$$

where $U_{elastic}$ is the elastic energy required to achieve conformality. The second term in Eq. 1 was introduced by Dalvi *et al.* (*7*) to account for the additional surface energy needed for PDMS to conform to the rough solid substrate. If the experiments are conducted in air or underwater, then the intrinsic (thermodynamic) work of adhesion, W_{int}, will be a function of the surface energies measured in air or underwater. In Eq. 2

$$(W_{int})_{\alpha} = \gamma_{S-\alpha} + \gamma_{PDMS-\alpha} - \gamma_{S-PDMS} \quad (2)$$

the symbol α is used to denote experiments conducted in air (A) or in water (L). We used subscript S for the diamond surface.

In Fig. 1C, we compare the experimentally measured values of W_{app} as a function of the predicted W_{app} as calculated using Eq. 1 for the experiments conducted in air. We used an average $\gamma_{PDMS-(A)}$ value of 23 mJ/m^2 based on values reported in the literature (*26*, *27*). The $U_{elastic}$ term was calculated with the Persson-Tosatti model using the PSDs for the rough diamond surfaces (fig. S3) and the four different moduli for PDMS (table S1). We used $(W_{int})_A$ as a fitting parameter and obtained a value of 41.9 ± 3.7 mJ/m^2 based on the highest R^2 value. This value is same as the thermodynamic limit for the two nonpolar solids that interact through dispersive interactions (*28*). In our previous publication, we obtained relatively lower W_{int} and R^2 values due to the calculation of area ratios (r_{true}) with a small slope assumption (*7*), while we have used the complete nonlinear expression (eq. S9) for calculating area ratios here. The high R^2 values we obtained strongly support the conclusion that the diamond/PDMS contact interface is conformal; thus, adhesion can be predicted using Eq. 1.

For underwater adhesion, $(W_{int})_L$ can be determined by measuring the water contact angle on PDMS, $(\theta_{PDMS-L})_A$, and on the smoothest diamond surface (PUNCD), $(\theta_{S-L})_A$ (*5*). This calculation yields the thermodynamic adhesion value for a dry contact created in underwater conditions. Combining Eq. 2 with the Young-Dupré equation yields

$$(W_{int})_L = (W_{int})_A - \gamma_{L-A}[\cos(\theta_{PDMS-L})_A + \cos(\theta_{S-L})_A] \quad (3)$$

the $(W_{int})_A$ value obtained from Fig. 1C and the measured water contact angles [$(\theta_{PDMS-L})_A = 105° \pm 2°$ and $(\theta_{S-L})_A = 99.6° \pm 1°$], we obtained a $(W_{int})_L$ of 73 mJ/m^2. This thermodynamic value is similar to the adhesion for hydrophobic PDMS in contact with a hydrophobic self-assembled monolayer or in contact with another PDMS surface under water (~75 mJ/m^2) (*6*). The interfacial energy $\gamma_{PDMS-(L)}$ of 41.8 mJ/m^2 is measured using the water contact angle on PDMS and Young's equation. Figure 1D shows a comparison between the experimental and theoretical predictions (Eq. 1) for W_{app} under water. The experimental values are much lower than those predicted by the Persson-Tosatti model for conformal contact, pointing toward a breakdown of the conformal contact model and the trapping of water.

In Fig. 2, we plotted the experimental underwater adhesion values measured in retraction ($W_{Pull-off}$). In these experiments, the lenses were retracted with a continuous velocity of 60 nm/s, and the work of adhesion during retraction was calculated using the JKR model (section S4 and equation S11). The adhesion values in retraction (pull-off) (table S5) were four to five times higher than those predicted from Eq. 1 (conformal contact model) and six to seven times higher than those experimentally measured during approach. Observing adhesion hysteresis (i.e., differences between approach and retraction) is not unusual for rough surfaces in dry environments (*7*).

Two common explanations for adhesion hysteresis (differences between adhesion energy measured during retraction and approach) are the viscoelasticity of elastomers and/or polarity of the solid substrates used in the JKR experiments. Here, we have measured the adhesion during approach and retraction cycles for PDMS lenses in contact with a low-energy smooth surface (section S1). Both approach and retraction data could be fitted using the JKR model with small hysteresis (table S1, less than 10 mJ/m^2). In addition, in this study, we have used low-energy diamond surfaces to ensure that the polar interactions are minimized. This indicates that the high adhesion hysteresis observed here was not caused by the viscoelasticity of the PDMS lenses nor polar interactions but instead could be due to

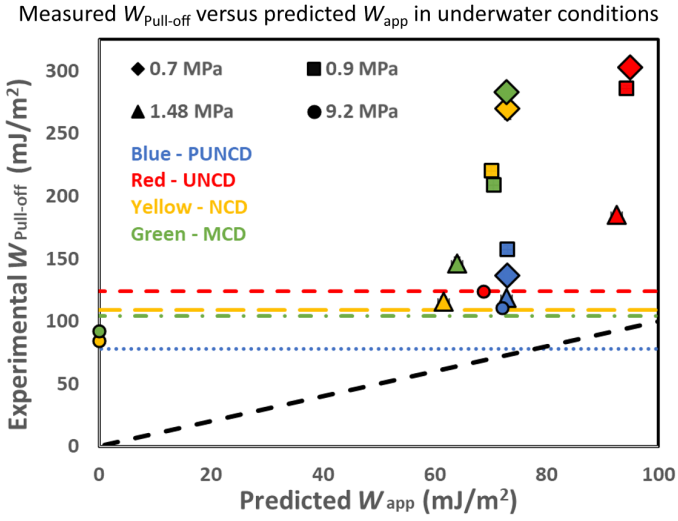

Fig. 2. Underwater work of adhesion during retraction compared with expectations from the thermodynamic work of adhesion. Experimental values for the pull-off work of adhesion are shown for PDMS against rough diamond surfaces as a function of predicted W_{app} (using Eq. 1). The values are also reported in table S5 (section S4). The horizontal lines (blue dotted for PUNCD, red double dashed for UNCD, yellow dashed for NCD, and green dash-dotted for MCD) show the upper limits on $W_{Pull-off}$, which are calculated by $(W_{int})_L r_{true}$, assuming that the contacts in retraction are conformal and lose energy for complete contact area due to roughness. The observation that most of the contacts show higher $W_{Pull-off}$ values as compared to Griffith's limit is supported by the energy loss (adhesion hysteresis) curves shown in fig. S6.

the roughness of the diamond surfaces. To check whether the high $W_{Pull-off}$ values in our underwater experiments arise due to roughness or increased area, we plotted the Griffith upper limit (horizontal lines in Fig. 2) for $W_{Pull-off}$, i.e., $(W_{int})_L r_{true}$. Griffith's values will be observed only if the two surfaces completely conform under water and if energy is lost due to roughness for the entire contact area (*7*). Unexpectedly, most $W_{Pull-off}$ values are even higher than the upper limit expected from Griffith's criteria. The combination of roughness and water leads to unexpected observations that are not explained by our current understanding.

To test the presence of water or the conformality of surfaces after contact formation, we performed surface-sensitive sum-frequency generation (SFG) spectroscopy of the contact interface between a rough surface (UNCD) and PDMS using the geometry shown in Fig. 3. The thin layer of UNCD was deposited on a sapphire prism, and SFG measurements were conducted using a total internal reflection geometry where the signals were not generated from the bulk phases (water, diamond, or PDMS) but only from the interface. Figure 3 shows SFG spectra for UNCD/air, UNCD/water, and UNCD in contact with the PDMS lens under water. For the UNCD/air interface, we observed peaks at 2838 and 2920 cm^{-1} that are assigned to the surface C—H stretching bands of monohydride H-terminated C(111) and C(001)-(2 × 1) reconstructed diamond crystallographic planes, respectively (*29*–*31*). A relatively small C—H stretching band at 2867 cm^{-1} originated from defects at grain boundaries or regions where the C(111) is partially H-terminated (*30*). The complete assignment of peaks in the SFG spectra is summarized in section S5 (table S6). The presence of multiple sharp C—H stretching bands demonstrates the polycrystalline nature and H-termination of the UNCD surface. The SFG spectroscopy in this geometry can result in signals from the diamond/sapphire interface as well. However, we do not anticipate any resonance signals from sapphire or nonhydrogenated diamond surfaces in this infrared (IR) region. Sapphire surfaces are typically decorated with surface OH groups, and the high-temperature process of the plasma-enhanced chemical vapor deposition (PECVD) process has resulted in removing those OH groups (as evident from no signals between 3500 and 3700 cm^{-1} in Fig. 3 collected in the presence of air).

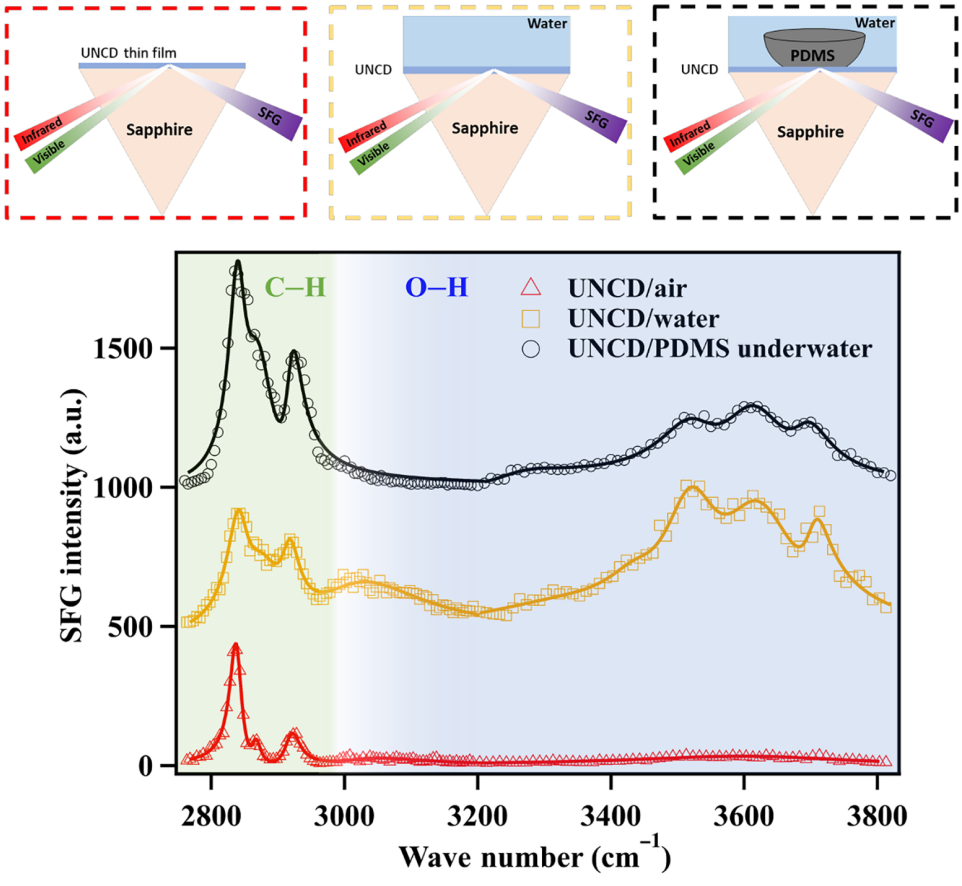

Fig. 3. Surface-sensitive spectroscopy results confirm the presence of trapped water and the nonconformal nature of the contact interface. SFG spectra for UNCD/air (red open triangles), UNCD/water (orange open squares), and UNCD/PDMS contact formed underwater (black open circles) interfaces in PPP (P-polarization SFG, P-polarization visible, and P-polarization IR). The images on top show three scenarios for which the SFG spectra were collected. UNCD thin film (~100 nm) was deposited on a sapphire prism using PECVD (details in section S2). The C—H (2750 to 3000 cm^{-1}) and O—H (3000 to 3800 cm^{-1}) vibrational stretching regions are shaded in light green and blue. The spectra are shown in arbitrary units (a.u.), and are vertically offset for visualization. All spectra are fitted with multiple peaks using the Lorentzian function (eq. S12), and the fitting parameters along with peak assignments are tabulated in table S6. The presence of water bands at the UNCD/PDMS interface under water (black open circles) reveals the nonconformal nature of the rough adhesive contact. We followed the same procedure for contact formation between the PECVD-coated sapphire prism and the PDMS lens as used in the adhesion measurements.

For the UNCD/water spectrum (Fig. 3), water-stretching bands in the 3000- to 3800-cm^{-1} region were observed in addition to the C—H bands. This region of the SFG spectrum reveals three populations of surface water molecules: strongly H-bonded water (3000 to 3200 cm^{-1}); H-bonded water, similar to that observed in liquid water (3200 to 3500 cm^{-1}); and weakly bonded water (3600 to 3800 cm^{-1}), particularly those with hydroxyl groups facing toward —CH groups on the diamond (hydrophobic) surface (*32*, *33*). After bringing PDMS in contact with UNCD underwater, we continued to observe water peaks between 3400 and 3800 cm^{-1}, confirming the nonconformal nature of contact with trapped water, which indicates a loss of molecular contact and qualitatively explains the differences observed between the experimental and theoretical adhesion values as shown in Fig. 1D. In the past, we have reported SFG measurements for the contact between two smooth surfaces underwater (*6*). For hydrophobic surfaces, as expected, we observed a completely dry contact and no traces of water signals in the SFG spectra. In contrast for PDMS in contact with a hydrophilic sapphire surface, we observed a nanometer-thin layer of trapped water. This technique is capable of distinguishing between dry and wet contact interfaces (*6*).

Our results indicate a nonconformal contact for soft elastomers in contact with rough diamond surfaces with trapped water. This trapped water results in a reduction in adhesion energy during approach and unexpectedly high adhesion during retraction. Next, we discuss a generalized adhesion model to predict underwater adhesion during approach and the role of heterogeneous contact in increasing the work of adhesion during retraction.

DISCUSSION

Trapped water reduces contact area during approach

To quantitatively explain the low adhesion observed during approach, we need to understand how to account for nonconformal contact. Here, we used the idea behind the Persson-Tosatti model to develop the following generalized adhesion model (Fig. 4A). This model is derived on the basis of the work per unit area, W_{app}, done to create a contact between an elastomer and a solid rough surface considering the surface energy and elastic energy required to deform the PDMS elastomer (the details of the derivation are discussed in section S6)

$$W_{app} = f_S(W_{int})_L - \gamma_{PDMS-L}(f_S + f_L - 1) - \frac{U_{elastic}(C^{new})}{A_{app}} \quad (4)$$

Since the contact is nonconformal, we defined the fraction of PDMS area in direct contact with diamond surfaces as $f_S = A_{PDMS-S}/A_{app}$ and the fraction in contact with water as $f_L = A_{PDMS-L}/A_{app}$, where A_{PDMS-S} and A_{PDMS-L} are the areas of PDMS in contact with diamond (solid) and water (liquid), respectively. The quantity $(f_S + f_L)$ is equal to the new surface area of PDMS after contact underwater, and this quantity is greater than or equal to 1. $U_{elastic}$ is the elastic term derived by the Persson-Tossati model, provided that we know the new PSD for the nonconformal PDMS contact. This generalized model (Eq. 4) reduces to a conformal model (Eq. 1) if we plug $f_L = 0$ and $f_S = r_{true}$. For nonconformal contacts, although Eq. 4 makes no approximation, it contains three terms that cannot be directly measured using only the adhesion data: f_S, f_L, and $U_{elastic}(C^{new})$. The terms $(W_{int})_L$ and γ_{PDMS-L} were determined experimentally and were found to be 73 and 41.8 mJ/m^2, respectively.

To reduce the unknown parameters in Eq. 4 by one, we assumed that the PDMS elastomer underwater contact with a diamond surface is similar to that of an uncross-linked PDMS liquid droplet in contact with a diamond surface underwater. The use of PDMS liquid ensures that this system is chemically identical to that of the PDMS elastomer. We expect that the trapped water is similar in both the elastic PDMS and the liquid PDMS contact interface because the process is controlled by the contact force generated due to adhesion rather than the external load (*34*, *35*). For smooth surfaces, past studies have shown that the adhesion energy measured using contact angles was comparable to those measured using mechanical measurements (*26*, *36*). Specifically, in a study carried out by Defante *et al.* (*6*), we showed that the adhesion energy measured using JKR measurements for PDMS in contact with a self-assembled n-octadecyltrichlorosilane (OTS) monolayer agreed with the adhesion energy measured using the Young-Dupré equation using liquid PDMS in contact with OTS monolayers. This direct comparison between the JKR model and the Young-Dupre equation assumes that the heterogeneity in the contact region is also reflected in the contact line (*6*). The contact angles, $(\theta_{PDMS-S})_L$, of liquid PDMS on the four rough diamond surfaces under water can be related to f_S and f_L using the Cassie-Baxter equation

$$\cos(\theta_{PDMS-S})_L = f_S\cos(\theta^*_{PDMS-S})_L - f_L \quad (5)$$

where the term $(\theta^*_{PDMS-S})_L$ is the thermodynamic contact angle of PDMS on a smooth diamond surface under water, as determined using the Young-Dupré equation and the PDMS-diamond underwater work of adhesion.

To obtain information about the two other unknown parameters in Eq. 4 requires additional simplifications. We hypothesized that the PDMS-water interface is flat; this allows us to relate A_{PDMS-L} to the projected area of the diamond-water interface A_{DW-P}, where A_{DW} is the area of the diamond surface in contact with water (fig. S5). This simplification is justified, as the hydrophobic PDMS would tend to minimize its area in contact with water, which would result in a flatter PDMS-water interface. In addition, we assume that the area ratios of the diamond surface are similar in dry and wet regions, which means that $A_{DW}/A_{DW-P} = A_{true}/A_{app} = r_{true}$. These simplifications allow us to write f_L as $A_{DW-P}/A_{app} = A_{DW}/(r_{true}A_{app}) = (A_{true} - A_{PDMS-s})/(r_{true}A_{app})$ which yields

$$f_L = 1 - \frac{f_S}{r_{true}} \quad (6)$$

We solved Eqs. 5 and 6 simultaneously for f_S and f_L, and the values are reported in Table 1. The new area ratio (A_{new}/A_{app}) of PDMS, which is equivalent to $(f_S + f_L)$, is also shown in Table 1.

The last unknown parameter in Eq. 4 is the energy stored in the deformed elastomer, $U_{elastic}(C^{new})$, which depends on the new PSD of the PDMS. Since there exist no experimental or theoretical approaches for calculating PSD, we plotted the comparison between the experimental results and the theoretical predictions for underwater W_{app} using Eq. 4 based on two limits for $U_{elastic}$.

The first limit is $U_{elastic}(C^{new}) = 0$, which represents no deformation of the PDMS elastomer (Fig. 4B). As anticipated, all the predicted W_{app} values are found to be higher than those observed experimentally as no elastic penalty is considered. The W_{app} without the elastic term (Table 1) is similar to W_{app} calculated using the Young-Dupré equation, $\gamma_{PDMS-L}[1 + (\theta_{PDMS-S})_L]$ (Table 1). One can

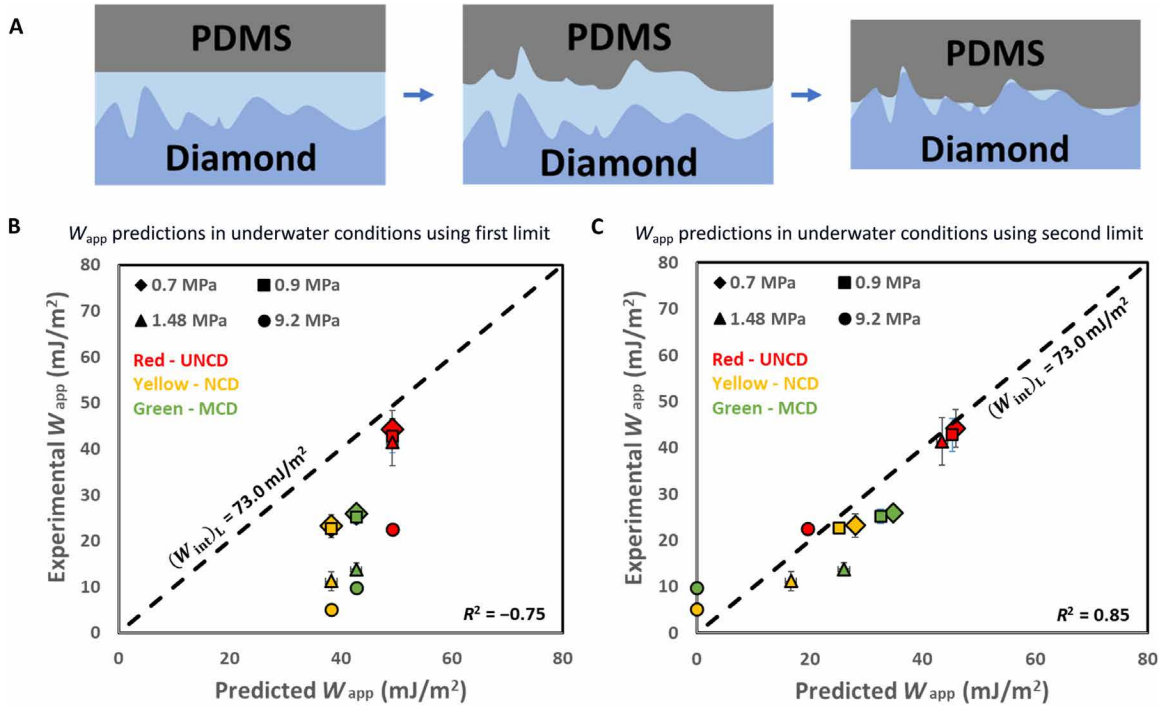

Fig. 4. Nonconformal adhesion model explains the loss of underwater adhesion during approach. To achieve partial contact under water, (**A**) the initial state (left) of the elastic body must undergo a change in area and store elastic strain energy as depicted by the intermediate state (middle). The underwater partial contact between PDMS elastomer and rough diamond substrates (right) results from water entrapment. Predictions of underwater adhesion using a generalized adhesion model (Eq. 4) with two limits on stored elastic strain energy: (**B**) Apparent work of adhesion as computed using $U_{elastic}(C^{new}) = 0$ (corresponding to the first limit in the main text) and (**C**) using the second limit, where $U_{elastic}(C^{new})$ is set to the value that is equal to the stored elastic strain energy when the contacts are conformal.

Table 1. Summary of dry and wet contact areas and work of adhesion calculated using Young-Dupré model. True area ratios were calculated using eqs. S8 and S9. PDMS contact angles were measured underwater for PDMS liquid in contact with rough diamond surfaces. Percolation thresholds for PDMS-solid contacts and new area ratios for PDMS in contact with diamond substrates are calculated using Eqs. 5 and 6. In addition, W_{app} calculated using the first two terms in Eq. 4 and work of adhesion calculated using the Young-Dupré equation for PDMS liquid-diamond contacts underwater are also reported. For PUNCD, no calculations were performed as the liquid PDMS shows a range of contact angles on PUNCD pointing toward an unstable contact interface.

Substrate	r_{true}	$(\theta_{PDMS-S})_L$	f_S	f_L	$\left(\frac{A_{new}}{A_{app}}\right)$	Dry percolation ($\phi_{Dry} = 1 - f_L$)	W_{app} (Eq. 4) with $U_{elastic}(C^{new}) = 0$	Work of adhesion Young-Dupré (mJ/m²)
PUNCD	1.07	59.7°– 83.0°	–	–	–	–	–	–
UNCD	1.70	79.6° ± 2.3°	0.88	0.48	1.36	0.52	49.2	49.3
NCD	1.49	94.7° ± 2.8°	0.65	0.55	1.20	0.45	39.1	38.4
MCD	1.43	88.7° ± 0.3°	0.71	0.51	1.22	0.49	42.6	42.7

show that first two terms in Eq. 4 are the same as the Young-Dupré equation for liquid PDMS in contact with rough surfaces underwater, provided that f_S and f_L are similar for a solid PDMS and liquid PDMS in contact with these rough diamond surfaces.

The second limit is the point where PDMS completely conforms to the diamond surface (Fig. 4C). For the case where $U_{elastic}(C^{new}) = U_{elastic}(C)$, C is the PSD of the rough diamond surface. We found an excellent agreement of the experimental results and the theoretical predictions if we use $U_{elastic}(C^{new}) = U_{elastic}(C)$. This observation is unexpected, since the use of a conformal limit on elastic energy in Eq. 4 would be inconsistent with the use of the area fractions, f_S and f_L, which predict that nearly 50% of the contact area contains trapped water.

To better understand these results, we plotted the normalized elastic strain energy $[U_{elastic}(q_{Cut})/U_{elastic}(C)]$ and new area ratio $[A_{new}(q_{Cut})/A_{true}(C)]$ of PDMS elastomer in nonconformal contact with four rough diamond surfaces as a function of q_{Cut} (the length scale until which the contacts are conforming) in Fig. 5A. We observed that $U_{elastic}$ reaches the values expected for conformal contact at much lower values of q_{Cut} as compared to the area ratio, consistent with the expectations that the elastic energy is controlled by smaller q or larger length scales (λ), while the area ratio is controlled by larger q or smaller length scales (λ). We also plotted the values of $(f_S + f_L)/r_{true}$ or A_{new}/A_{true} from Table 1 to find where they intercept with the predictions of the area ratio (Fig. 5A). The intercepts occur at values of q_{Cut} where the elastic ratio is close to 1 (vertical dashed

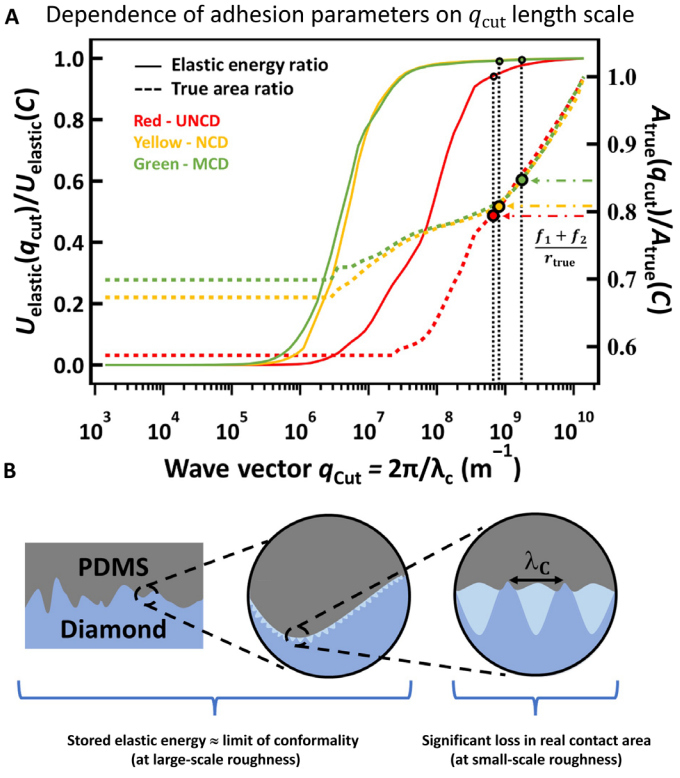

Fig. 5. Water entrapment in nanometer-scale asperities decreases the work of adhesion during approach. (**A**) Normalized elastic strain energy and new area ratio are plotted as a function of the wave vector integrated between q_L (lower limit) to q_{Cut} (table S7). The horizontal dashed arrows show the Cassie-Baxter predictions for the area ratios of PDMS elastomer, and vertical dotted lines represent the q_{Cut} where those area ratios are achieved. The vertical dotted lines drawn at those particular q_{Cut} values are extended to estimate the fraction of stored elastic energy in PDMS that is conformal at each length scale. Open circles on the elastic energy curves demonstrate the q_{Cut} values at which the stored elastic energy is saturated. This understanding of the dependence of adhesion parameters on length scale helped in visualizing a simple contact model. (**B**) At lower magnifications, the elastic contact seems to conform perfectly; however, at the smaller length scales, water becomes entrapped when the q_{Cut} is exceeded.

lines; values reported in table S7), supporting the argument that a large fraction of the high-q asperities (nano-asperities) are wet, while the smaller-q asperities form conformal contacts (fig. 5B).

Trapped water increases the adhesion during retraction

The results indicating that the retraction adhesion values are much higher than the expected thermodynamic values are very intriguing, considering that nearly 50% of the contact area is in contact with water. The increase in underwater adhesion during retraction cannot be accounted for by the roughness-induced energy loss or by the increased area (Griffith-like model), as had previously been suggested to explain the adhesion hysteresis for dry contacts (*7*). In fig. S6 (section S8), we show the energy loss for underwater contacts as a function of the true contact area. For underwater contacts, the energy loss points lie above Griffith's limit (i.e., the energy loss expected for complete conformal contact). The upper limit should also be an overestimation, since a substantial fraction of the area is wet, and the wet regions would disrupt molecular interactions. Therefore, it is puzzling why the crack cannot just propagate into the liquid-filled region and reduce adhesion during retraction.

A recent model explains the origin behind higher adhesion during retraction for soft elastomers in contact with rough surfaces in dry conditions due to pinning of the contact line (*8*, *9*). In this model, the variation in local values of work of adhesion leads to pinning of the interface and enhanced adhesion hysteresis. The pinning model would predict that the adhesion hysteresis, specifically the difference in W_{app} between approach and retraction, should increase with an increase in $U_{elastic}$. For the case of underwater adhesion, we observe an opposite trend [fig. S7 (section S9)] where adhesion hysteresis decreases as a function of $U_{elastic}$. Both lower modulus and less-rough surfaces enhance adhesion hysteresis. This indicates the need for considering hydrodynamic and capillary effects with pinning in explaining the retraction data.

The unusual trend with trapped water has been observed to increase friction against smooth surfaces (*6*, *21*). In this past example, it was anticipated that a partially wet contact region should have low friction compared to a completely dry contact when these friction experiments were conducted under water. Instead, they observed the opposite case where the friction was higher for a partially wet contact compared to a dry contact. In those experiments, roughness also enhances underwater adhesion during retraction by almost a factor of four compared to the thermodynamic work of adhesion based on surface chemistry (*21*). For dry adhesion, patterned heterogeneity has also been exploited to increase pull-off forces (*37*, *38*).

Last, we want to discuss the possibility that the nonconformal contact could be due to low-density phase pockets (nanobubbles) reported to form next to hydrophobic surfaces (*39*). Bubbling nitrogen is expected to reduce the amount of dissolved oxygen and reduce the formation of nanobubbles, which is the procedure used here (*39*). Studies using x-ray reflectivity and SFG on stable hydrophobic surfaces in contact with water do not show any evidence for nanobubbles (*40*–*42*). The SFG results presented here confirm the presence of trapped water, instead of trapped nanobubbles. However, the question remains whether these low-density pockets are formed during retraction. Both the presence of water pockets or water vapor–rich pockets would result in heterogeneous contact and would enhance adhesion hysteresis and raise adhesion during pull-off. A theoretical model that considers all these factors to explain the retraction results is the focus of our future work.

In summary, we have measured the underwater adhesion between PDMS elastomers and well-characterized rough diamond surfaces. By comparing the extracted work of adhesion during approach with a nonconformal contact adhesion model, we showed that water is trapped in 10-nm-scale asperities between the soft hydrophobic elastomer and the rough diamond substrates. Both the reduced contact area and the elastic energy required to deform the elastomer explain the reduction in adhesion energy during approach. However, this effect of trapped water occupying almost 50% of the apparent contact area serves to increase the adhesion during retraction by nearly a factor of four above the thermodynamic work of adhesion. These results reveal the inadequacy of dry contact models to describe wet contacts and demonstrate the alternative mechanisms that govern underwater adhesion. This work highlights opportunities for designing surfaces with controlled topography and surface chemistry to optimize the performance of adhesives for use in wet environments. There exist intriguing examples in nature that use topology and chemistry to either increase or decrease

adhesion under water and in humid conditions (*14*, *15*, *43*–*46*); this work provides rigorous experimental results and a simple numerical model that may explain the science behind these adaptations.

MATERIALS AND METHODS

Rough polycrystalline diamond surface preparation and characterization

UNCD, MCD, and NCD substrates were prepared by chemical vapor deposition using the parameters described elsewhere (*47*, *48*). PUNCD was obtained by performing chemical mechanical planarization. The as-received diamond samples were hydrogenated in microwave plasma. The details of these processes as well as the recipe and process conditions for preparing the UNCD-coated sapphire prism for SFG spectroscopy are provided in section S2. The surface chemistry of these diamond substrates was characterized by collecting x-ray photoelectron spectroscopy survey scans (shown in fig. S1) and measuring the water contact angle and contact angle hysteresis (reported in table S2). In addition, the surface roughness was characterized across all length scales, and the resulting roughness parameters are provided in table S3 (section S3). SFG spectroscopy of the UNCD-coated sapphire prism was carried out for three contact interfaces as shown in Fig. 3. Details for the SFG spectroscopy and the corresponding fitting parameters for the spectra are provided in section S5.

Underwater adhesion measurements

The JKR contact mechanics experiments were performed using the custom-built setup shown in Fig. 1A. Millipore water (with a volume resistivity of 18.2 megohm·cm) used in the experiments was deaerated with nitrogen to remove the dissolved oxygen and reduce the possibility of cavity formation during PDMS/diamond (hydrophobic-hydrophobic) contact (*39*). Optically clear hemispherical PDMS lenses and rough diamond surfaces were submerged under the surface of the water before the start of the experiments. The dimensions of the hemispherical PDMS lenses were selected in such a way that the radius (1.2 to 1.4 mm) was below the capillary length of PDMS, and the height (greater than 700 μm) was sufficient to prevent the transfer of stress from the lenses to the glass arm holding the lenses (*5*, *49*). The stage holding the diamond surface was moved toward the PDMS lens at a velocity of 60 nm/s using a stepper motor. In-situ measurements of contact force (P) and contact radius (a) were carried out. Experimental a^3 versus P data for 16 different PDMS/diamond contacts were plotted and fitted to eq. S10 (section S4) to extract E^* (effective modulus) and W_{app} (apparent/observed work of adhesion). E^* depends on the elastic moduli of the two materials in contact and their Poisson ratios: $1/E^* = (1-\nu^2_{PDMS})/E_{PDMS} + (1-\nu^2_{Diamond})/E_{Diamond}$. For rigid diamond substrates, the quantity $E_{Diamond}$ tends to infinity. Using the Poisson's ratio for PDMS, ν_{PDMS} of 0.5 (for perfect elastic systems), the E_{PDMS} can be calculated. The large refractive index difference between diamond ($n_1 = 2.4$) and PDMS ($n_2 = 1.43$) provided the contrast to measure the contact area underwater by collecting scattered light. The contacts were loaded in a stepwise fashion to a force of 1 mN. A 1-min equilibration time was given at each step to allow the system to stabilize.

Underwater PDMS contact angle on rough diamond surfaces

The diamond substrates were immersed under deaerated Millipore water in a transparent quartz container. Sessile drops of uncured PDMS polymers (DMS V-05, V-21 and V-31 from Gelest Inc.) were pumped through a glass syringe and brought into contact with the diamond substrates under water. The adhesive forces were adequate to pull down a PDMS droplet. The contact angle reached an equilibrium within 10 s after bringing the PDMS droplet into contact with the diamond surfaces. We collected the contact angles using a goniometer (DSA100E, KRUSS) after an elapsed time of 30 s. To confirm the stability of the measured contact angles, the system was disturbed by tapping the goniometer stage by hand and poking a metal needle into the PDMS. The underwater PDMS contact angles on rough diamond surfaces were found to be stable and are reported in Table 1 as $(\theta_{PDMS-S})_L$. The effect of molecular weight and viscosity of PDMS polymer on the measured equilibrium contact angles was negligible.

Supplementary Materials

This PDF file includes:

Sections S1 to S9
Figs. S1 to S7
Tables S1 to S7
References

REFERENCES AND NOTES

1. C. Cai, Z. Chen, Y. Chen, H. Li, Z. Yang, H. Liu, Mechanisms and applications of bioinspired underwater/wet adhesives. *J. Polym. Sci.* **59**, 2911–2945 (2021).
2. J. H. Waite, Mussel adhesion–essential footwork. *J. Exp. Biol.* **220**, 517–530 (2017).
3. A. Y. Stark, I. Badge, N. A. Wucinich, T. W. Sullivan, P. H. Niewiarowski, A. Dhinojwala, Surface wettability plays a significant role in gecko adhesion underwater. *Proc. Natl. Acad. Sci. U.S.A.* **110**, 6340–6345 (2013).
4. A. Y. Stark, J. Ohlemacher, A. Knight, P. H. Niewiarowski, Run don't walk: Locomotor performance of geckos on wet substrates. *J. Exp. Biol.* **218**, 2435–2441 (2015).
5. M. Sun, N. Kumar, A. Dhinojwala, H. King, Attractive forces slow contact formation between deformable bodies underwater. *Proc. Natl. Acad. Sci. U.S.A.* **118**, e2104975118 (2021).
6. A. P. Defante, T. N. Burai, M. L. Becker, A. Dhinojwala, Consequences of Water between Two Hydrophobic Surfaces on Adhesion and Wetting. *Langmuir* **31**, 2398–2406 (2015).
7. S. Dalvi, A. Gujrati, S. R. Khanal, L. Pastewka, A. Dhinojwala, T. D. B. Jacobs, Linking energy loss in soft adhesion to surface roughness. *Proc. Natl. Acad. Sci. U.S.A.* **116**, 25484–25490 (2019).
8. A. Sanner, L. Pastewka, Crack-front model for adhesion of soft elastic spheres with chemical heterogeneity. *J. Mech. Phys. Solids* **160**, 104781 (2022).
9. A. Sanner, N. Kumar, A. Dhinojwala, T. D. B. Jacobs, L. Pastewka, Why soft contacts are stickier when breaking than when making them. *Sci. Adv.* **10**, eadl1277 (2024).
10. A. A. Griffith VI, "The phenomena of rupture and flow in solids" in *Philosophical Transactions of the Royal Society of London. Series A, Containing Papers of a Mathematical or Physical Character* (Royal Society; 1921), vol. 221, pp. 163–198.
11. D.-M. Drotlef, L. Stepien, M. Kappl, W. J. P. Barnes, H.-J. Butt, A. del Campo, Insights into the adhesive mechanisms of tree frogs using artificial mimics. *Adv. Funct. Mater.* **23**, 1137–1146 (2013).
12. A. M. Smith, Cephalopod sucker design and the physical limits to negative pressure. *J. Exp. Biol.* **199**, 949–958 (1996).
13. A. M. Smith, The role of suction in the adhesion of limpets. *J. Exp. Biol.* **161**, 151–169 (1991).
14. D. K. Wainwright, T. Kleinteich, A. Kleinteich, S. N. Gorb, A. P. Summers, Stick tight: Suction adhesion on irregular surfaces in the northern clingfish. *Biol. Lett.* **9**, 20130234 (2013).
15. F. Tramacere, L. Beccai, M. Kuba, A. Gozzi, A. Bifone, B. Mazzolai, The morphology and adhesion mechanism of octopus vulgaris suckers. *PLOS ONE* **8**, e65074 (2013).
16. W. Li, X. Yang, P. Lai, L. Shang, Bio-inspired adhesive hydrogel for biomedicine—Principles and design strategies. *Smart Medicine* **1**, e20220024 (2022).
17. Y. Wang, R. Hensel, Bioinspired underwater adhesion to rough substrates by cavity collapse of cupped microstructures. *Adv. Funct. Mater.* **31**, 2101787 (2021).
18. A. Tiwari, B. Persson, Physics of suction cups. *Soft. Matter* **15**, 9482–9499 (2019).
19. A. Lin, R. Brunner, P. Chen, F. Talke, M. Meyers, Underwater adhesion of abalone: The role of van der Waals and capillary forces. *Acta Mater.* **57**, 4178–4185 (2009).
20. N. Hosoda, S. N. Gorb, Underwater locomotion in a terrestrial beetle: Combination of surface de-wetting and capillary forces. *Proc. Biol. Sci.* **279**, 4236–4242 (2012).
21. A. P. Defante, A. Nyarko, S. Kaur, T. N. Burai, A. Dhinojwala, Interstitial water enhances sliding friction. *Langmuir* **34**, 4084–4094 (2018).

22. A. Gujrati, A. Sanner, S. R. Khanal, N. Moldovan, H. Zeng, L. Pastewka, T. D. B. Jacobs, Comprehensive topography characterization of polycrystalline diamond coatings. *Surf. Topogr.* **9**, 014003 (2021).
23. B. N. J. Persson, E. Tosatti, The effect of surface roughness on the adhesion of elastic solids. *J. Chem. Phys.* **115**, 5597–5610 (2001).
24. A. V. Sumant, D. S. Grierson, J. E. Gerbi, J. Birrell, U. D. Lanke, O. Auciello, J. A. Carlisle, R. W. Carpick, Toward the ultimate tribological interface: Surface chemistry and nanotribology of ultrananocrystalline diamond. *Adv. Mater.* **17**, 1039–1045 (2005).
25. K. L. Johnson, K. Kendall, A. Roberts, Surface energy and the contact of elastic solids. *Proc. R. Soc. Lond. A.* **324**, 301–313 (1971).
26. M. K. Chaudhury, G. M. Whitesides, Direct measurement of interfacial interactions between semispherical lenses and flat sheets of poly (dimethylsiloxane) and their chemical derivatives. *Langmuir* **7**, 1013–1025 (1991).
27. M. K. Chaudhury, Interfacial interaction between low-energy surfaces. *Mater. Sci. Eng. R. Rep.* **16**, 97–159 (1996).
28. M. K. Chaudhury, T. Weaver, C. Hui, E. Kramer, Adhesive contact of cylindrical lens and a flat sheet. *J. Appl. Phys.* **80**, 30–37 (1996).
29. R. J. Cannara, M. J. Brukman, K. Cimatu, A. V. Sumant, S. Baldelli, R. W. Carpick, Nanoscale friction varied by isotopic shifting of surface vibrational frequencies. *Science* **318**, 780–783 (2007).
30. R. Chin, J. Y. Huang, Y. Shen, T. Chuang, H. Seki, Interaction of atomic hydrogen with the diamond C (111) surface studied by infrared-visible sum-frequency-generation spectroscopy. *Phys. Rev. B* **52**, 5985–5995 (1995).
31. H.-C. Chang, J.-C. Lin, J.-Y. Wu, K.-H. Chen, Infrared spectroscopy and vibrational relaxation of CHx and CDx stretches on synthetic diamond nanocrystal surfaces. *J. Phys. Chem.* **99**, 11081–11088 (1995).
32. Q. Du, E. Freysz, Y. R. Shen, Surface vibrational spectroscopic studies of hydrogen bonding and hydrophobicity. *Science* **264**, 826–828 (1994).
33. F. Perakis, L. De Marco, A. Shalit, F. Tang, Z. R. Kann, T. D. Kühne, R. Torre, M. Bonn, Y. Nagata, Vibrational spectroscopy and dynamics of water. *Chem. Rev.* **116**, 7590–7607 (2016).
34. B. N. J. Persson, Contact mechanics for randomly rough surfaces. *Surf. Sci. Rep.* **61**, 201–227 (2006).
35. B. Persson, Adhesion between an elastic body and a randomly rough hard surface. *Eur. Phys. J. E.* **8**, 385–401 (2002).
36. M. K. Chaudhury, G. M. Whitesides, Correlation between surface free energy and surface constitution. *Science* **255**, 1230–1232 (1992).
37. N. J. Glassmaker, A. Jagota, C.-Y. Hui, W. L. Noderer, M. K. Chaudhury, Biologically inspired crack trapping for enhanced adhesion. *Proc. Natl. Acad. Sci. U.S.A.* **104**, 10786–10791 (2007).
38. M. K. Chaudhury, A. Chakrabarti, A. Ghatak, Adhesion-induced instabilities and pattern formation in thin films of elastomers and gels. *Eur. Phys. J. E.* **38**, 82 (2015).
39. E. E. Meyer, K. J. Rosenberg, J. Israelachvili, Recent progress in understanding hydrophobic interactions. *Proc. Natl. Acad. Sci. U.S.A.* **103**, 15739–15746 (2006).
40. A. Poynor, L. Hong, I. K. Robinson, S. Granick, Z. Zhang, P. A. Fenter, How water meets a hydrophobic surface. *Phys. Rev. Lett.* **97**, 266101 (2006).
41. E. Tyrode, J. F. D. Liljeblad, Water structure next to ordered and disordered hydrophobic silane monolayers: A vibrational sum frequency spectroscopy study. *J. Phys. Chem. C* **117**, 1780–1790 (2013).
42. B. M. Ocko, A. Dhinojwala, J. Daillant, Comment on "How Water Meets a Hydrophobic Surface". *Phys. Rev. Lett.* **101**, 039601 (2008).
43. D. M. Green, D. L. Barber, The ventral adhesive disc of the clingfish gobiesox maeandricus: Integumental structure and adhesive mechanisms. *Can. J. Zool.* **66**, 1610–1619 (1988).
44. A. M. Smith, S. M. LaValva, M. M. Loiacono, J. T. Thompson, Suction adhesion in the gliding joint of a cephalopod. *J. Exp. Biol.* **223**, jeb211227 (2019).
45. W. M. Kier, A. M. Smith, The structure and adhesive mechanism of octopus suckers. *Integr. Comp. Biol.* **42**, 1146–1153 (2002).
46. V. Kang, R. Johnston, T. van de Kamp, T. Faragó, W. Federle, Morphology of powerful suction organs from blepharicerid larvae living in raging torrents. *BMC Zoology* **4**, 10 (2019).
47. H. Zeng, A. R. Konicek, N. Moldovan, F. Mangolini, T. Jacobs, I. Wylie, P. U. Arumugam, S. Siddiqui, R. W. Carpick, J. A. Carlisle, Boron-doped ultrananocrystalline diamond synthesized with an H-rich/Ar-lean gas system. *Carbon* **84**, 103–117 (2015).
48. J. E. Butler, A. V. Sumant, The CVD of nanodiamond materials. *Chem. Vap. Depos.* **14**, 145–160 (2008).
49. M. Deruelle, H. Hervet, G. Jandeau, L. Léger, Some remarks on JKR experiments. *J. Adhes. Sci. Technol.* **12**, 225–247 (1998).
50. S. Kaur, A. Narayanan, S. Dalvi, Q. Liu, A. Joy, A. Dhinojwala, Direct observation of the interplay of catechol binding and polymer hydrophobicity in a mussel-inspired elastomeric adhesive. *ACS Cent. Sci.* **4**, 1420–1429 (2018).
51. S. Perutz, E. J. Kramer, J. Baney, C.-Y. Hui, C. Cohen, Investigation of adhesion hysteresis in poly(dimethylsiloxane) networks using the JKR technique. *J. Polym. Sci. B* **36**, 2129–2139 (1998).
52. A. Gujrati, S. R. Khanal, L. Pastewka, T. D. Jacobs, Combining TEM, AFM, and profilometry for quantitative topography characterization across all scales. *ACS Appl. Mater. Interfaces* **10**, 29169–29178 (2018).
53. K. L. Johnson, J. A. Greenwood, An adhesion map for the contact of elastic spheres. *J. Colloid Interface Sci.* **192**, 326–333 (1997).
54. D. Maugis, Adhesion of spheres: The JKR-DMT transition using a dugdale model. *J. Colloid Interface Sci.* **150**, 243–269 (1992).
55. A. G. Lambert, P. B. Davies, D. J. Neivandt, Implementing the theory of sum frequency generation vibrational spectroscopy: A tutorial review. *Appl. Spectrosc. Rev.* **40**, 103–145 (2005).

Acknowledgments: We thank B. N. J. Persson and M. Muser for insightful discussions on the parameters that control percolation and underwater adhesion. We thank H. King and L. Strathmann for helpful comments and discussion. We thank S. Merriman, U. Patil, and S. Kumar at the University of Akron for input on the manuscript. **Funding:** We thank the Center of Nanoscale Materials (Argonne National Laboratory) for supporting this research under proposal #76145. A.D. acknowledges the financial support from the National Science Foundation (NSF DMR 2208464). Work performed at the Center for Nanoscale Materials, a US Department of Energy Office of Science User Facility, was supported by the US DOE, Office of Basic Energy Sciences, under contract no. DE-AC02-06CH11357. A.D. also acknowledges funding from Knight Foundation (W. Gerald Austen Endowed Chair). **Author contributions:** N.K. and A.D. designed the research; N.K. performed the adhesion and spectroscopy experiments; A.V.S. synthesized and H-terminated rough diamond surfaces; N.K. performed the calculations and derived the nonconformal adhesion model; N.K., S.D., A.V.S., L.P., T.D.B.J., and A.D. discussed the results; N.K. and A.D. wrote the manuscript; N.K., S.D., A.V.S., L.P., T.D.B.J., and A.D. reviewed and edited the manuscript. **Competing interests:** The authors declare that they have no competing interests. **Data and materials availability:** Experimental adhesion data, JKR fitting parameters, raw SFG data used to create Fig. 2, power spectral densities (PSDs) of the four rough diamond surfaces, and summary sheets containing results for dry and underwater adhesion measurements have been deposited on Zenodo and can be accessed at https://doi.org/10.5281/zenodo.10975362. All other data needed to evaluate the conclusions in the paper are present in the paper and/or the Supplementary Materials.

Submitted 2 January 2024
Accepted 2 July 2024
Published 7 August 2024
10.1126/sciadv.adn8343